biomass

MDPI

*Article*

# Exploring Biomass Waste-Derived Biochar as a Catalyst for Levulinic Acid Conversion to γ-Valerolactone: Insights into Synthesis, Characterization, and Catalytic Performance

**Joao Carlos Alves Macedo [1,*], Maryam Shirinkar [2], Richard Landers [3] and André Henrique Rosa [2,*]**

[1] Institute of Chemistry, São Paulo State University (UNESP), Araraquara 14800-060, Brazil
[2] Institute of Science and Technology, São Paulo State University (UNESP), Sorocaba 18087-180, Brazil; maryam.shirinkar@unesp.br
[3] Surface Physics Group, Department of Applied Physics, "Gleb Wataghin" Institute of Physics, University of Campinas, Campinas 13083-859, Brazil; landers@ifi.unicamp.br
* Correspondence: j.macedo@unesp.br (J.C.A.M.); andre.rosa@unesp.br (A.H.R.); Tel.: +34-645465-000 (J.C.A.M.)

**Abstract:** The transition from fossil resources to renewable raw materials derived from lignocellulosic waste is crucial for economic and environmental sustainability. Advancing toward a bio-based economy necessitates the development of innovative heterogeneous catalysts. This study explores the use of modified sugarcane bagasse biochar, embedded with ruthenium and iron particles, as a green catalyst for converting levulinic acid (LA) to γ-valerolactone (GVL). The efficiency of both raw and modified biochar in the LA to GVL conversion process, utilizing formic acid (FA) exclusively as the hydrogen source, was systematically assessed through characterization techniques, including XRD, TGA, XPS, and SEM/EDS. The gelification method using alginate enhanced the ruthenium and iron content on the surface of the biochar. The results demonstrate that the modified material has significant potential for efficient LA-to-GVL conversion, achieving a yield of 73.0 ± 9.2% under optimized conditions (0.5 g of $BC_{500}Fe/3\%Ru$ at 180 °C for 3 h, with 4 mmol LA, 8 mmol FA, and 10 mL of water). Iron on the biochar surface facilitated the formation of adsorption sites for LA, supporting the notion of this novel catalyst for LA conversion in an aqueous medium in the presence of FA. This research underscores the potential of this green catalyst in advancing sustainable biomass conversion and contributes to the ongoing shift towards a bio-based economy.

**Keywords:** catalyst; biochar; ruthenium; iron; valerolactone; levulinic acid

check for updates

Academic Editor: Carlo Pastore

Received: 27 March 2025
Revised: 5 May 2025
Accepted: 8 May 2025
Published: 17 May 2025

**Citation:** Macedo, J.C.A.; Shirinkar, M.; Landers, R.; Rosa, A.H. Exploring Biomass Waste-Derived Biochar as a Catalyst for Levulinic Acid Conversion to γ-Valerolactone: Insights into Synthesis, Characterization, and Catalytic Performance. *Biomass* **2025**, *5*, 29. https://doi.org/10.3390/biomass5020029

**Copyright:** © 2025 by the authors. Licensee MDPI, Basel, Switzerland. This article is an open access article distributed under the terms and conditions of the Creative Commons Attribution (CC BY) license (https://creativecommons.org/licenses/by/4.0/).

## 1. Introduction

In the 21st century, there has been an exponential increase in industrial and economic growth. The chemical industry, heavily reliant on fossil fuels (coal, oil, and gas), has witnessed the establishment of petrochemicals and refineries as dominant entities within this sector [1]. Given the finite nature of fossil fuel resources, coupled with their high price volatility and uneven global distribution, there is a pressing need to intensify the search for alternative resources [2].

A comprehensive assessment of the reserves/production (R/P) ratio, as per the British Petroleum Statistical Review on World Energy 2021, indicates approximately 139 years of remaining coal production and around 50 years for oil and gas production [3]. The extensive exploration and utilization of fossil resources for heat, energy, and chemical

production have not only contributed to the resource scarcity but have also generated various environmental impacts, including the release of $CO_2$ into the atmosphere [4].

Consequently, there is a critical imperative to pursue sustainable development by utilizing environmentally benign resources capable of yielding heat, energy, and chemical products equivalent to those derived from fossil resources [5]. Lignocellulosic biomass residues emerge as a viable and sustainable resource, characterized by their easy accessibility and renewability, offering the potential to generate equivalent heat, energy, and chemical products [6].

The industrial conversion of lignocellulosic biomass residues into value-added products holds great significance, enabling the production of platform chemicals that are renewable, easily accessible, safe, low in toxicity, and biodegradable [7]. $\gamma$-valerolactone (GVL) stands out as one of the most promising platform molecules due to its low toxicity, high boiling point, and favorable biodegradation properties. GVL can be further transformed into fuel additives, green solvents, food additives, and intermediates for the chemical and pharmaceutical industries [8]. The global GVL market is experiencing substantial growth as industries increasingly prioritize sustainable and eco-friendly practices. The growing demand for bio-based solvents and chemicals, along with the drive for cleaner alternatives in chemical manufacturing, has propelled the market for GVL.

Levulinic acid (LA) is a promising intermediate in the production of GVL. It is obtained through the hydrolysis of the cellulosic fraction of lignocellulosic biomass. The United States Department of Energy has recognized LA as one of the top ten most promising platform chemicals for future biorefineries. Owing to its carboxyl and carbonyl functional groups, LA serves as a versatile precursor for the synthesis of various value-added compounds, including GVL [9].

The synthesis of GVL involves the reaction between LA and formic acid (FA), with FA serving as the hydrogen source for the subsequent conversion of LA into GVL, as described in Figure 1 [10].

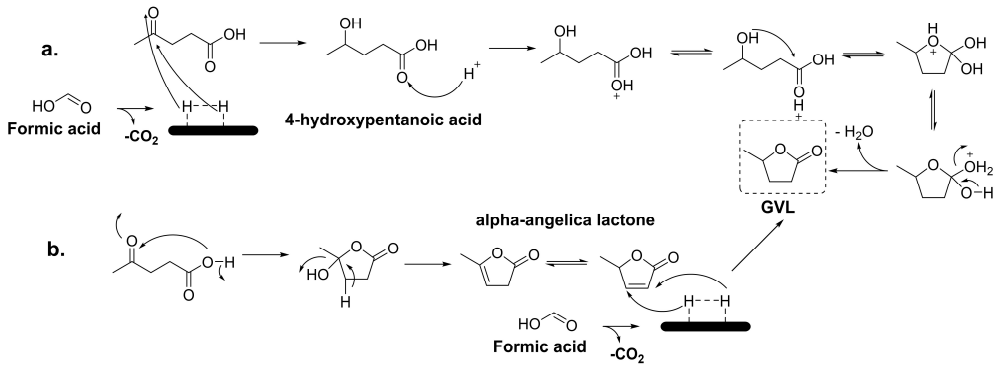



**Figure 1.** Schematic representation of the formation of GVL by the formation routes of the intermediates (**a**) 4-hydroxypentanoic acid or (**b**) $\alpha$-angelica lactone, from the decomposition of FA and reaction with LA.

Notably, studies have traditionally employed hydrogen gas, a fossil source, for the hydrogenation of LA using FA in conjunction with a catalyst, which presents an alternative hydrogen source for GVL synthesis [11]. Ruthenium (Ru) has emerged as a commonly utilized metallic catalyst due to its superior activity compared to catalysts based on palladium and platinum, albeit at a higher purchase cost [12].

Gao et al. (2018) addressed the challenge of catalyst stability in the hydrogenation of LA with FA, developing Ru-supported catalysts. Their findings underscored the efficacy of the $Ru/ZrO_2$ catalyst, specifically with a Ru content below 3% ($m/m$), prepared through a sol–gel process and doping with 0.1% $SiO_2$ to enhance its stability and enable catalyst

recycling. The stability concerns were attributed to the acidic conditions of the conversion reaction, leading to formic acid decomposition on Ru, generating CO that poisons the catalyst [13].

To improve the catalyst's stability, there is a growing emphasis on developing stable heterogeneous catalysts that incorporate metallic particles within their structure, primarily due to their enhanced recovery capacity [14]. Catalysts supported by carbon-based materials like graphene, activated carbon, and biochar, among others, have been shown to address the problem of leaching, albeit at the cost of catalyst regeneration [15].

In the pursuit of a comprehensive biomass utilization strategy within the biorefinery processes, biochar serves as a valuable support material for metallic particles in the development of heterogeneous catalysts. The favorable structural and functional characteristics of biochar, including surface properties, porosity, and functional groups, make it an ideal support material, especially considering its status as a by-product of biomass thermochemical conversion [16].

Despite the significant advantages of biochar as a catalytic support, its application in catalysts has been scarcely explored. Therefore, further studies are necessary to assess its potential, particularly in biomass conversion reactions aimed at producing value-added products. In this context, the main objective of this work was the preparation and investigation of novel biochar-supported bimetallic heterogeneous catalysts for use in the selective hydrogenation of LA to obtain GVL.

Hence, the primary objective of this study was to synthesize a bimetallic catalyst (Fe/Ru) supported by biochar particles, whilst varying the pyrolysis temperatures and ruthenium contents. The second focus of this research involved the application of synthesized catalysts in the production of GVL from LA using FA as a hydrogen source in water as the solvent. This study presents a report on GVL production via the dehydration/hydrogenation of LA in the absence of hydrogen gas, employing biochar-supported metal catalysts. The results obtained contribute to a better understanding of the role of biochar as a catalytic support, opening new perspectives for sustainable biomass conversion processes.

## 2. Materials and Methods

### *2.1. Reagents*

The levulinic acid (natural, 99%), formic acid (p.a., ACS reagent, reag. Ph. Eur., ≥98%), triethylamine (p.a., ≥99.5% (GC)), ruthenium(III) chloride hydrate (ReagentPlus®), $\gamma$-valerolactone (≥99%, FCC, FG) were purchased from Sigma-Aldrich (São Paulo, Brazil), iron sulfate pentahydrate (p.a.), sodium formate (≥99.10% Neon), sodium alginate (p.a.), and ethyl acetate (HPLC Plus, for HPLC, GC, and residue analysis, 99.9%) were purchased from Labsynth for preparation. The sugarcane bagasse biomass utilized in this study was sourced from sugarcane juice vendors in Sorocaba, São Paulo, Brazil.

### *2.2. Synthesis of Biochar-Supported Ru/Fe Particles*

The biochar-supported Ru/Fe particles were prepared employing a methodology akin to that described by Wang et al. [17]. For the synthesis of bead-type adsorbent, the "gelation-pyrolysis" process was implemented as follows: 6 g of sugarcane bagasse biomass (BM), previously dried at room temperature, crushed in a knife mill, and standardized to 35 mesh, was blended with 200 mL of $RuCl_3$ solution (1%, 3%, and 5% ($w/w$)) at 25 °C. Following 2 h of agitation, 0.4 g (2% $w/v$) of sodium alginate was dissolved in the solution, and the resulting mixed slurries were dripped into $FeSO_4 \cdot 7H_2O$ solution (5% $w/v$) using a dropper. After immersion in the solution for 18 h for hardening, the hydrogel was filtered and thoroughly dried at 50 °C for 12 h. Following the drying process, the granular biomass

was transferred to sealed crucibles and placed within a stainless steel annular reactor with a volume of 0.82 $cm^3$. Before thermal treatment, the reactor was purged with nitrogen gas for 15 min to establish an inert atmosphere. Subsequently, the samples were subjected to a sequential temperature program, increasing from ambient to 300 °C, 500 °C, and 700 °C at a controlled heating rate of 5 °C $min^{-1}$. The furnace was maintained at the target temperature for 2 h (retention time), followed by cooling to room temperature for over 12 h (overnight). The stainless steel tubular reactor ensures a controlled, low-oxygen atmosphere crucial for biomass pyrolysis and biochar production through a robust sealing system at its ends. This configuration prevents air ingress, promoting thermal decomposition without combustion.

The resulting products were denoted as $BC_{300}$Fe/1%Ru, $BC_{300}$Fe/5%Ru, $BC_{500}$Fe/3%Ru, $BC_{700}$Fe/1%Ru, and $BC_{700}$Fe/5%Ru.

Additionally, to assess the influence of the catalyst on the mass transfer performance during synthesis, raw biochar was subjected to a range of temperatures (300 °C, 500 °C, and 700 °C), resulting in $BC_{300}$, $BC_{500}$, and $BC_{700}$. $BC_{500}$3%Ru was obtained by mixing bagasse sugarcane (BM) with $RuCl_3$ 3% (*m*/*m*) solution; the suspension was dried at 80 °C for 12 h and pyrolyzed at 500 °C. All the catalysts underwent triple washing with a 1% HCl solution and deionized water, were dried at 80 °C, ground into a powder, and are summarized in Table S1, and the fabrication process of BC-Fe/Ru is illustrated in Figure S1.

### 2.3. Material Characterization

The catalyst samples underwent comprehensive characterization through scanning electron microscopy (SEM) and Energy Dispersive X-ray Spectroscopy (EDS) using an Analytical Scanning Electron Microscope (JEOL JSM-6010LA-Unesp Campus Sorocaba—Sorocaba, Brazil). This characterization aimed to observe the surface morphology, determine the structural features, and qualitatively analyze the surface elemental composition of the catalysts. The crystallized phases of the catalyst powders were examined using a powder X-ray diffractometer (XRD X Panalytical X'Pert Powder—Unesp campus Sorocaba—Brazil) with Cu/K$\alpha$ radiation ($\lambda$ = 1.5418 Å).

Thermogravimetric analysis (TGA) of the samples was conducted using TA Instrument apparatus with a simultaneous differential thermal analysis–thermogravimetric analysis (DTA-TGA) thermal analyzer, at a temperature of 700 °C with a heating rate of 10 °C/min.

The surface elemental composition analysis of the biochar-supported catalyst (BC) was carried out using X-ray photoelectron spectroscopy (XPS). Detailed descriptions of the techniques and experimental procedures employed for the characterization are provided in the Supplementary Materials (Method S1).

### 2.4. Effect of Temperature Pyrolysis on the GVL Production

An initial evaluation was conducted to compare various catalysts and ascertain the optimal pyrolysis temperature. A 25 mL autoclave hydrothermal reactor was charged with 10 mL of water, 4 mmol of LA, and 8 mmol FA, along with 0.5 g of $BC_x$Fe/y%Ru (x = pyrolysis temperature; y = Ru content) to facilitate the reaction. The reaction took place in an oil bath equipped with a magnetic stirrer, with the temperature varied up to 160 °C, over 120 min.

After the reaction, the contents within the reactor were easily recovered with the assistance of an external magnet. The separated aliquots were diluted in 25 mL of water and subjected to liquid–liquid extraction using ethyl acetate (2 mL/2 mL) as per the method outlined by Serrano-Ruiz et al. (2010) [18], facilitating further analysis.

### *2.5. Statistical Analysis of GVL Production with $BC_{500}Fe/3\%Ru$ as the Catalyst*

#### 2.5.1. Fractional Factorial Design

To enhance the efficacy of the study, the experimental methodology employed a fractional factorial design $2^{4-1}$, encompassing 8 experiments, with more than 3 trials designated as central points. The objective was to assess the impact of various factors on the ultimate yield of the product, considering modifications in the controlled variables during the synthesis process, namely reaction time, reaction temperature, FA/LA ratio, and catalyst mass. Each factor was characterized by lower and higher values denoted as lower level (−1), medium, and higher level (+1), as delineated in Tables S2 and S3. The acquired data underwent scrutiny using Design-Expert 11, Excel v.2023, and Octave 8.4.0 software for comprehensive analysis.

In an autoclave hydrothermal reactor (25 mL), a mixture consisting of 10 mL of water, 4 mmol of LA, and varying quantities of FA (4, 12, and 20 mmol) was prepared, along with predetermined amounts of $BC_{500}Fe/3\%Ru$ (0.02, 0.06, and 0.1 g) to facilitate the reaction. The reaction was conducted in an oil bath on a hot plate equipped with a magnetic stirrer, with temperature variations (120, 150, and 180 °C) over different durations (2, 3, and 4 h). Following the specified reaction duration, the hydrothermal reactor was removed and rapidly cooled to room temperature via immersion in cold water.

Post-reaction, the reactor contents were separated and recovered easily with the assistance of an external magnet for subsequent analyses. Aliquots of the separated phases were diluted in water and subjected to liquid–liquid extraction using ethyl acetate (2 mL/2 mL) for GC-MS analysis, following the methodology described by Serrano-Ruiz et al. (2010) [18].

#### 2.5.2. Response Surface of the Central Composite

The central composite methodology, implemented through response surface analysis, was employed to identify the optimal conditions for GVL production utilizing $BC_{500}Fe/3\%Ru$ as the catalyst. The application of this methodology involved the utilization of Design-Expert 11, Excel, and Octave software. Based on the fractional factorial design analysis, the investigation focused on the impact of two independent variables, namely the reaction temperature and catalyst mass, recognized as critical factors influencing the GVL yield. These variables were encoded at four levels: −1.4, −1, 0, +1, and +1.4 (as detailed in Tables S4 and S5). A total of 11 experiments were conducted, with constant parameters including a solvent volume of 10 mL, a reaction time of 3 h, and a fixed FA/LA ratio (2–8/4 mmol).

The mathematical associations between the independent variables and the yield of GVL production were delineated by modeling the experimental data in a quadratic form, expressed as Equation (1):

$$CY(\%) = \beta_0 + \beta_1 X_1 + \beta_2 X_2 + \beta_{11} X_1^2 + \beta_{22} X_2^2 \beta_{12} X_1 X_2, \quad (1)$$

where $Y$ is the yield of GVL production; $\beta_0$ is a constant; $\beta_1$ and $\beta_2$ are linear coefficients; $\beta_{11}$ and $\beta_{22}$ are the quadratic coefficients; $\beta_{12}$ is the interaction coefficient of variables 1 and 2; $X_1$ and $X_2$ are independent variables [19]. Statistical significance was determined at the 95% confidence level.

### *2.6. Analysis of the Hydrogenation Products of LA*

Aliquots of the samples underwent analysis using a gas chromatograph (Agilent 7890A-Unesp campus Sorocaba—Brazil) equipped with a bonded phase SPB-5 capillary column (5% polydiphenyl/95% polydimethylsiloxane, 30 μm × 0.25 mm × 0.25 μm, Sigma-Aldrich) and coupled to an ion trap mass spectrometer (Agilent 5975C MSD). A 1 μL volume of the sample was injected into the GC-MS instrument. The instrument operated

under the following temperature program: an initial temperature of 70 °C held for 3 min, followed by a heating ramp from 70 to 200 °C at a rate of 45 °C $min^{-1}$, maintained at 200 °C for 3 min. The helium flow was set at 1.5 mL $min^{-1}$, with a split ratio of 1:150, and inlet and GC/MS transfer line temperatures were maintained at 220 °C. Mass spectra were acquired at 70 eV using an ion trap analyzer, with a scan rate of 1 scan $s^{-1}$ over the range of 30 to 350 $m/z$. The resulting chromatogram exhibited a retention time of 4.72 min for GVL, and the mass spectrum displayed characteristic fragments at 56, 85, and 100 $m/z$, corresponding to the GVL molecule.

The catalytic outcomes are expressed about the yield of GVL. The GVL yield, quantified as moles of GVL formed per initial mole of the substrate, is defined by Equation (2):

$$\text{Yield GVL } (\%) = \left( \frac{\text{Formed mol of GVL}}{\text{Initial mol of LA}} \right) \times 100, \quad (2)$$

### *2.7. Cost Estimates*

Cost estimates were compiled in Microsoft Excel v.16 using the spreadsheet version of CatCost v.1.1.0 and the site https://catcost.chemcatbio.org, accessed on 12 December 2024 [20,21].

## 3. Results and Discussion

### *3.1. $BC_xFe/y\%Ru$ Catalyst Characterization*

The surface morphologies of the modified biochar were investigated through SEM imaging (Figure S2), and the EDS analysis (Figure 2) revealed the principal surface elements of BCxFe/y%Ru to be C, N, O, Fe, S, and Ru.

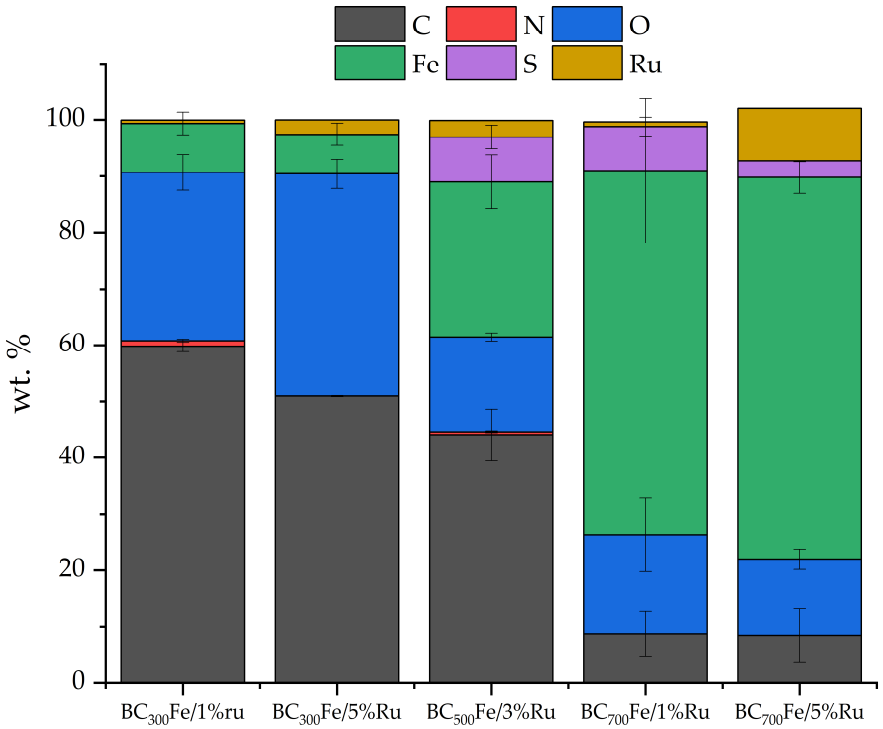



**Figure 2.** Elemental composition of the $BC_{300}Fe/1\%Ru$, $BC_{300}Fe/5\%Ru$, $BC_{500}Fe/3\%Ru$, $BC_{700}Fe/1\%Ru$, and $BC_{700}Fe/5\%Ru$.

However, the images and distribution maps in Figure S2, $BC_{300}Fe/1\%Ru$, $BC_{300}Fe/5\%Ru$, and $BC_{500}Fe/3\%Ru$ samples exhibit notable similarity to the original biomass, with preserved vessel elements. Also, Figure S2d,e of $BC_{700}Fe/1\%Ru$ and $BC_{700}Fe/5\%Ru$ samples depict a surface covered with ferric oxide, potentially obstructing the porous

structure [22]. The substantial presence of ferric oxide is corroborated by Figure 2, indicating an Fe content (%) of 64.73 ± 12.85 and 67.82 ± 2.83 in the surface composition, respectively.

We observed that samples pyrolyzed at 300 °C and 500 °C exhibited a significant carbon content (Figure 1), while those pyrolyzed at 700 °C showed markedly lower levels, comparable to residual ash. This trend indicates that the presence of Ru and Fe in biomass pyrolysis promotes a reduction in the carbon content with increasing temperature. Ruthenium appears to facilitate the removal of oxygen as $H_2O$ or $CO_2$ via deoxygenation reactions. This oxygen removal is concomitant with the breakdown of carbonaceous structures, leading to carbon loss in the form of gaseous compounds.

As shown in Figure 3, the diffractograms of the $BC_{500}Fe/3\%Ru$ sample exhibit a series of intense peaks, consistent with the presence of $Fe(OH)_2$, $Fe(OH)_3$, $Fe_2O_3$, and $Fe_3O_4$ [23,24]. Specifically, diffraction peaks at 30.2°, 35.6°, 43.2°, 53.8°, 57.3°, and 62.9° correspond to the six indexed planes (206), (119), (0012), (012), (104), and (4012) of $Fe_2O_3$, the predominant crystalline phase in $BC_{500}Fe/3\%Ru$ [25,26]. These peaks affirm the successful impregnation of Fe into the biochar, occurring during the gelification stage of the sugarcane–ruthenium–sodium alginate biomass suspension in the 5% $Fe^{2+}$ solution. In this process, Fe binds up to two carboxylic groups on adjacent alginate molecules [27].

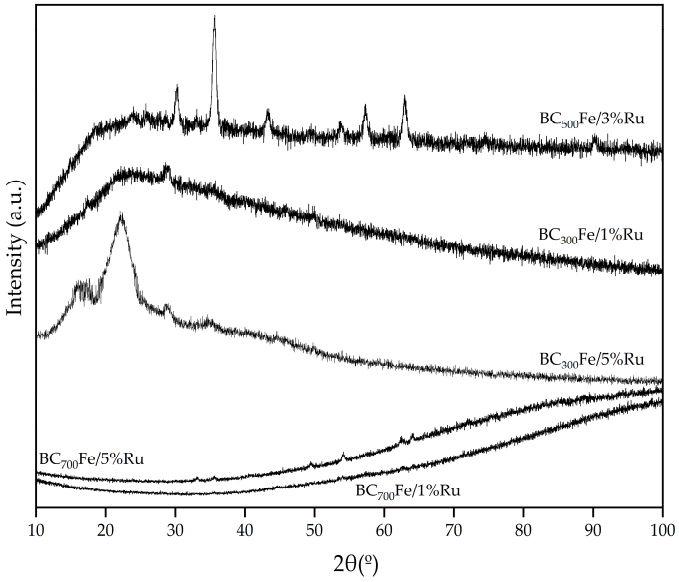



**Figure 3.** The diffractogram of $BC_{300}Fe/1\%Ru$, $BC_{300}Fe/5\%Ru$, $BC_{500}Fe/3\%Ru$, $BC_{700}Fe/1\%Ru$, and $BC_{700}Fe/5\%Ru$.

Contrastingly, the diffractograms of $BC_{700}Fe/1\%Ru$ and $BC_{700}Fe/5\%Ru$ exhibit an absence of distinct diffraction peaks, indicating that the synthesized materials lack crystallinity and are predominantly amorphous [28].

Characteristic diffraction peaks associated with Ru were not evident in the diffractogram profiles of all the examined samples. This observation may be attributed to the well-dispersed nature of Ru particles in the biochar matrix, the amorphous character of Ru in the catalysts, or the relatively low Ru content in the catalysts [5,29].

The deconvolution of the C1s, O1s, Fe3p, Ru3d, and S2p XPS spectra for the $BC_{300}Fe/1\%Ru$, $BC_{300}Fe/5\%Ru$, $BC_{500}Fe/3\%Ru$, $BC_{700}Fe/1\%Ru$, and $BC_{700}Fe/5\%Ru$ samples, is illustrated in Figure S3 and summarized in Table S6. The discernible peaks originating from Fe and Ru atoms in the XPS spectra of all the modified samples attest to the successful impregnation of Fe and Ru within the biochar.

The C1s spectra were subjected to tripartite deconvolution, with the peak at 284.6 eV in C1s assigned to C=C bonds, the range of 286.1–286.9 eV to C-OR, and 288.6–288.9 eV

to C-OOR. Notably, $BC_{500}Fe/3\%Ru$ exhibited an additional peak at 291.0 eV, attributed to π-π* vibration satellite peaks originating from the excitation of pi orbitals during photoemission [30,31]. Materials pyrolyzed at 300 °C and 500 °C displayed a reduction between 13–40% in the fraction of C=C after ruthenium/iron impregnation, which is likely due to the interactions between the carbon framework and ruthenium during biochar pyrolysis [32].

The deconvolution of the Ru3d curve revealed two well-separated doublets at 280.9–282.6 eV (assigned to $Ru3d_{5/2}$) and 284.8–286.8 eV (assigned to $Ru3d_{3/2}$), indicative of the presence of $RuO_2$ [32–34]. $BC_{700}Fe/5\%Ru$ also exhibited peaks at 280.6 and 284.8 eV, associated with the reduction of $RuO_2$ into metallic Ru [32].

The Fe2p spectra displayed peaks at 709.3–710.5 eV ($2p_{3/2}$ of $Fe^{2+}$) and 712.1–713.7.4 eV ($2p_{3/2}$ of $Fe^{3+}$), indicating the presence of both $Fe^{2+}$ and $Fe^{3+}$ in the $BC_{300}Fe/1\%Ru$, $BC_{300}Fe/5\%Ru$, $BC_{700}Fe/1\%Ru$, and $BC_{700}Fe/5\%Ru$ samples [35]. In $BC_{500}Fe/3\%Ru$, the XPS spectra located at 711.0 eV ($Fe2p_{3/2}$) suggest the presence of $Fe^{3+}$ cations, indicating the absence of the $Fe_3O_4$ phase and supporting the presence of $Fe_2O_3$ crystals [36], corroborated by the XRD analysis results.

The O1s peaks (Figure S3) at 528.0 eV, 530.0–530.1 eV, 531.5–531.9 eV, 532.0–532.6 eV, and 533.1–534.1 eV in all the samples are associated with the oxygen species related to Fe–O, O-Ru, O-H, C-O, and C=O bonds and hydrogen interaction with the $H_2O$, respectively. To understand the O1s peaks, further studies are necessary because the materials contain a variety of oxides with very similar energy values.

Moreover, the thermal stability analysis of $BC_{300}Fe/1\%Ru$, $BC_{300}Fe/5\%Ru$, $BC_{700}Fe/1\%Ru$, and $BC_{700}Fe/5\%Ru$ is displayed via the curves of TG and DTG in Figure 4a,b, respectively.

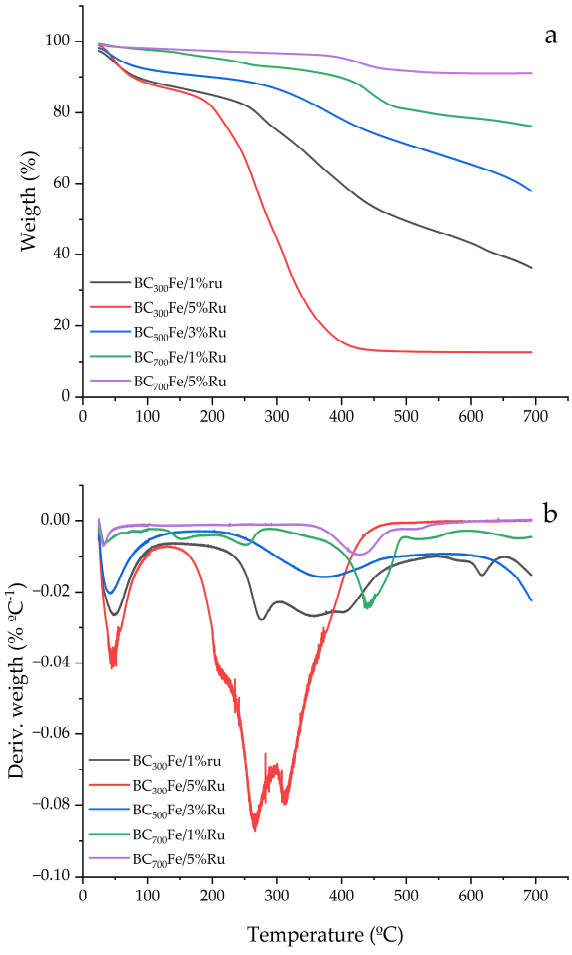



**Figure 4.** The (**a**) DTG and (**b**) TGA curves of $BC_{300}Fe/1\%Ru$, $BC_{300}Fe/5\%Ru$, $BC_{500}Fe/3\%Ru$, $BC_{700}Fe/1\%Ru$, and $BC_{700}Fe/5\%Ru$ samples.

Below 200 °C, all the samples exhibited weight loss (1.91–12.05%), attributed to the evaporation of the moisture content in the samples. The weight loss around 275 °C in $BC_{300}Fe/1\%Ru$ and $BC_{300}Fe/5\%Ru$ is attributed to the decomposition of cellulose and the degradation of lignin fractions [37].

Notably, the $BC_{500}Fe/3\%Ru$, $BC_{700}Fe/1\%Ru$, and $BC_{700}Fe/5\%Ru$ samples displayed weight losses between 367 °C and 440 °C in the DTG curve, indicative of the devolatilization of organic matter [37]. The absence of an exothermic peak around 275 °C in the $BC_{500}Fe/3\%Ru$, $BC_{700}Fe/1\%Ru$, and $BC_{700}Fe/5\%Ru$ samples suggests that the decomposition of hemicellulose and/or cellulose fractions occurred at elevated temperatures of pyrolysis.

### *3.2. Effect of the Temperature Pyrolysis on the GVL Production*

Catalytic experiments involving $BC_xFe/Ru$ samples produced at different pyrolysis temperatures (Figure 5) revealed that $BC_{500}Fe/3\%Ru$ exhibited the highest catalytic activity for GVL production. The enhanced catalytic activity of $BC_{500}Fe/3\%Ru$ could be attributed to its lower Ru content compared to $BC_{300}Fe/1\%Ru$ and $BC_{300}Fe/5\%Ru$. It was observed that the solution turned brown after each reaction, indicating potential leaching of Ru and/or Fe.

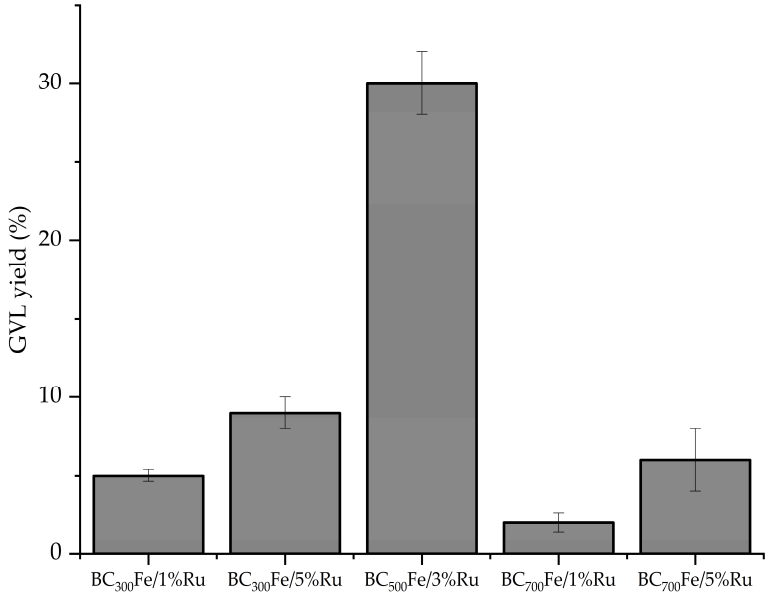



**Figure 5.** Effect of the temperature pyrolysis on the GVL production. Conditions for catalysis experiments: 4 mmol LA, 8 mmol FA, 0.5 g of sample catalysts, 160 °C for 2 h contact time.

As outlined by Su et al. (2023) [38], the Fe/C mass ratio plays a crucial role in influencing the structure, pore distribution of iron/composites, and consequently, the catalytic activities. The materials, $BC_{300}Fe/1\%Ru$, $BC_{300}Fe/5\%Ru$, $BC_{500}Fe/3\%Ru$, $BC_{700}Fe/1\%Ru$, and $BC_{700}Fe/5\%Ru$, exhibited C/Fe values of 0.14, 0.14, 0.62, 7.42, and 8.03, respectively (from Figure 2). Notably, $BC_{500}Fe/3\%Ru$ displayed an intermediate Fe/C value, suggesting a more even distribution of the ratio, thereby increasing the surface area of biochar and providing more contact points for catalysis [38].

Moreover, $BC_{700}Fe/1\%Ru$ and $BC_{700}Fe/5\%Ru$ exhibited surfaces covered by iron oxide, potentially contributing to the irregular shape of biochar, and shielding the porous structure and active sites [38].

Furthermore, the presence of iron on the biochar surface appears to enhance the LA adsorption, which could play a crucial role in the catalytic mechanism, potentially contributing to the improved reaction efficiency.

### *3.3. Statistical Analysis of GVL Production with $BC_{500}Fe/3\%Ru$ as the Catalyst*

#### 3.3.1. Fractional Factorial Design

A fractional factorial design was implemented for the synthesis of GVL from LA using formic acid as a hydrogen source in water as the solvent, with $BC_{500}Fe/3\%Ru$ serving as the catalyst. As outlined in Table S2, four factors were systematically considered for this investigation. The employed design, with a designated resolution, facilitated the determination of both the main effects and their interactions. The impact of each variable on the responses, specifically the GVL production, was assessed through the Pareto chart of standardized effects.

As illustrated in Figure S4, the influence of the four factors and their four-way interactions exhibited variations in response. Concerning the main effects on the response, the reaction temperature (°C—X1) emerged as the most influential variable, with catalyst mass (g—X3) following closely in significance.

The positive values of the effects associated with variables X1 and X3 signify that transitioning from the lower level (−1) to the higher level (+1) of these variables contributes to an elevation in GVL production. Consequently, it is advisable to operate within the region corresponding to the highest level of these variables, as depicted in Figure S5.

Elevated temperatures have been demonstrated to effectively enhance the selectivity and increase the GVL production, as substantiated by the previous findings [39]. The observed rise in the rate of $H_2$ generation from formic acid at higher temperatures may favor the conversion of LA to GVL [39,40]. The escalating GVL production with an increase in catalyst dosage can be predominantly attributed to the greater availability of catalytically active sites [41]. This suggests that the $BC_{500}Fe/3\%Ru$ catalyst effectively provided enough active hydrogenation sites, facilitating the highly selective conversion.

As per the fractional factorial design analysis, the effects of the reaction temperature and catalyst mass emerged as significant factors influencing the yield of GVL production.

#### 3.3.2. Response Surface of the Central Composite

To assess the impact of the reaction temperature and catalyst mass, the surface response is graphically represented in Figure 6. A discernible trend reveals a progressive augmentation in GVL production with elevated levels of both the reaction temperature and catalyst mass.

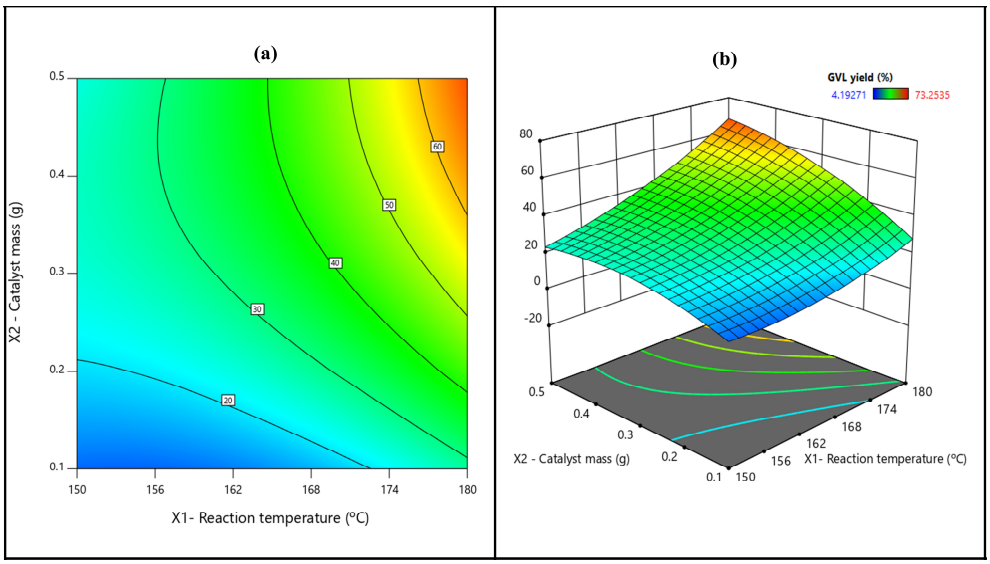



**Figure 6.** Contour (**a**) and surface response (**b**) chart of the effect of reaction temperature and catalyst mass.

For each of the two variables depicted in Figure 6, the analysis of variance (ANOVA) results (Table S7) reveals that all the variables exert a significant effect ($p$-value < 0.05). The calculated F value (Table S7) surpasses the tabulated F value (0.05; 5 = 2.57), signifying the model's significance with only a 0.16% chance that such a large F-value could occur due to noise. Consequently, the model effectively describes the catalytic process. The independent variables, ranked in decreasing order of influence on the model based on their significance ($p < 0.05$) and F-values (higher values of F and lower $p$-values), are X1, X2, and $X2^2$. The independent variables X1X2 and $X1^2$ are not significant at the 0.05 level but are close enough to suggest potential effects.

The model's accuracy, indicated by a value of 15.62, surpasses the desirable threshold of 4, and the lack of fit was deemed insignificant [42]. The coefficients of determination ($R^2$) and $R^2$-adjusted are 0.96 and 0.92, respectively. These $R^2$ values, approaching unity, signify a high correlation between the observed and predicted values [43].

The responses acquired were modeled using a quadratic equation to establish a correlation between the reaction conditions and GVL production. The resulting second-order equation for GVL production in terms of coded factors and non-coding is expressed by Equations (3) and (4):

$$Y\ (\%) = 34.05 + 15.29X_1 + 13.08X_2\ + 5.28X_1^2\ - 6.63X_2^2\ + 6.82X_1\ X_2\ , \quad (3)$$

$$Y\ (\%) = 582.64 - 7.40X_1 - 210.2X_2\ + 0.023X_1^2 - 165.64X_2^2\ + 2.27X_1\ X_2, \quad (4)$$

The response surface analysis aimed to predict the optimal reaction temperature and catalyst mass concentrations for achieving maximum GVL production. Utilizing Equations (3) and (4) for optimization, the solution with the highest desirability value was selected. The analysis determined that the optimal conditions for the reaction temperature and catalyst mass were 180 °C and 0.5 g, respectively, while keeping the other parameters (volume solvent, reaction time, and ratio FA/LA) constant at 10 mL, 3 h, and 2–8/4 mmol, respectively. The model predicted a GVL production yield of 67.88%. Experimentally, the obtained yield was 73 ± 9.2%, consistent with the value reported by [44] Rodríguez et al. (2023) [44].

The validation results of the optimum conditions are presented in Table S8. A two-tailed $t$-test analysis ($\alpha = 0.05$) was conducted to assess the statistical significance of the obtained values compared to the predicted responses from the respective models. The calculated $p$-value of 1.59 indicates no significant difference between the experimental condition results and the predicted responses from the models. These results affirm the validity of the model predictions.

The tests indicated that the $BC_{500}$3%Ru could be a viable alternative for LA-to-GVL conversion. However, future studies should focus on enhancing the catalyst's stability, evaluating its performance under various operational conditions, and assessing its potential for pilot-scale applications.

### *3.4. Control Catalyst Samples*

Under the optimized reaction conditions, an examination was conducted of the control catalysts ($BC_{500}$, $Fe_{500}$, $BC_{500}$3%Ru, and $BC_{500}$Fe), all prepared at a pyrolysis temperature of 500 °C, and subsequently utilized in the optimized reaction conditions as delineated in Section 3.2. The comparative analysis with the control catalysts is presented in Figure 7.

In the presence of $BC_{500}$3%Ru and $BC_{500}$Fe catalysts, LA was exclusively formed, whereas GVL emerged as the predominant or sole product when utilizing the bimetallic catalyst, $BC_{500}$Fe/3%Ru (Figure S6). This observation aligns with the findings generated by Ibrahim et al. (2023) [45] who reported similar outcomes using copper-based bimetallic catalysts.

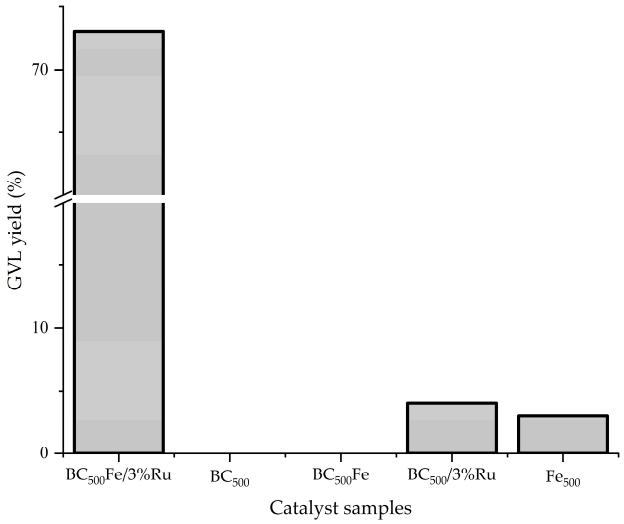



**Figure 7.** Validation of optimum conditions and comparison with control catalyst samples. Conditions for catalysis experiments: 4 mmol LA, 8 mmol FA, 0.5 g of sample catalysts, 180 °C for 3 h contact time.

Under the optimized reaction conditions, $BC_{500}$ and $BC_{500}Fe$ exhibited negligible catalytic activity, attributed to the absence of catalytic sites, specifically metallic Ru/Fe particles responsible for the decomposition of FA and the generation of $H_2$. $Fe_{500}$ samples yielded only a 3% GVL yield, indicative of the material lacking Ru particles crucial for hydrogen dissociation in the active centers.

$BC_{500}3\%Ru$, akin to $Fe_{500}$ samples, yielded a mere 4% GVL, emphasizing that Ru sites primarily serve for hydrogen dissociation, while the hydrogenation process likely transpires on the surface of $Fe_2O_3$. The latter provides adsorption sites for LA and functions as the reaction area for hydrogenation, as proposed by Jing et al. (2019) [46].

These findings underscore the potential of $BC_{500}Fe/3\%Ru$ in the hydrogenation of LA to GVL. Figure 8 depicts the proposed synergy between Ru-Fe sites in $BC_{500}Fe/3\%Ru$ and LA hydrogenation.

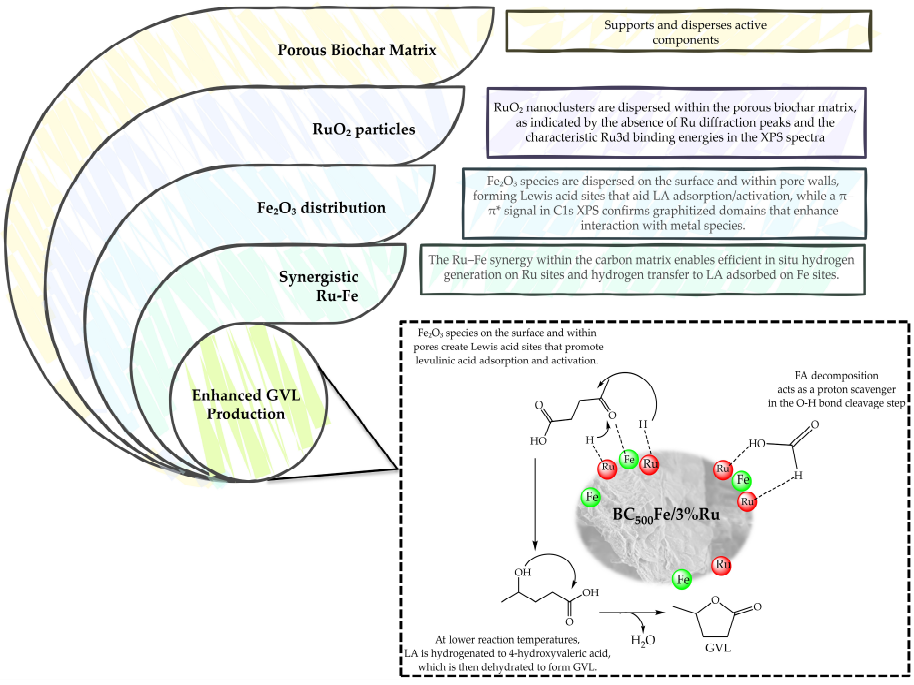



**Figure 8.** Schematic diagram to describe the synergy of Ru-Fe sites of $BC_{500}Fe/3\%Ru$ in LA hydrogenation.

### *3.5. Recyclability of $BC_{500}$Fe/3%Ru Catalysts*

The recyclability of the $BC_{500}$Fe/3%Ru catalyst system was assessed under the optimized conditions, as depicted in Figure 9. Following each reaction cycle, the catalyst underwent separation from the products and was subjected to reuse after a treatment involving washing with water, filtration, and drying at 60 °C for 2 h. In the first three cycles, no noticeable decline in catalytic activity was observed. However, in cycles 4 and 5, there was a reduction in catalytic activity, with respective decreases of 16% and 34% in the yield of GVL. Thus, after five cycles of catalyst use, a discernible decline in catalytic activity became evident. This reduction is likely attributed to the loss of catalyst mass during the catalyst recovery process in the autoclave reactor.

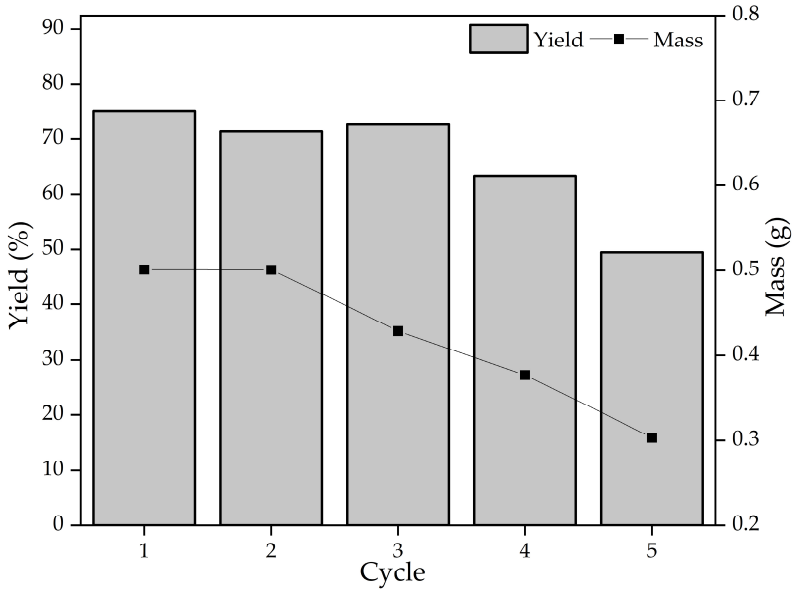



**Figure 9.** Catalytic recyclability studies for the $BC_{500}$3%Ru. Conditions: 4 mmol LA, 8 mmol FA, 0.5 g $BC_{500}$Fe/3%Ru, 180 °C, 3 h.

The reduction in the mass of the catalyst during recovery processes, via extraction through filtration, water washing, and subsequent drying, has been described as a phenomenon akin to that expounded by Shi et al. (2023) [47]. This phenomenon decreases the catalytic efficacy of the catalyst upon each iterative cycle of deployment, attributed to the recuperation of the catalyst throughout the extraction and separation procedure's post-reaction [47], a phenomenon concomitantly observed in the present study.

By the fifth cycle, the catalyst's mass had a high diminished recovery, accompanied by a reduction in the yield of GVL. This indicates that the loss of mass during the tests could be a contributing factor to the decrease in the GVL yield.

### *3.6. Investigation of Metal Leaching*

A series of Ru- and/or Fe-biochar catalysts were prepared for the hydrogenation of LA, and Fe-Ru leaching was studied via ICP-OES analysis (Table 1).

Variations in Ru and Fe metal leaching were observed among the different catalyst compositions. $BC_{500}$Ru exhibited the maximum Ru leaching at 0.00050 wt%, while $BC_{500}$Fe3%Ru displayed a lower Ru leaching of 0.00026 wt%. This outcome suggests that the presence of Fe in the $BC_{500}$Fe3%Ru formulation contributed to the solubilization and stabilization of Ru particles in the catalyst. Fortunately, Ru leaching remained negligible for all the catalyst samples, with values ranging between 0.00018 and 0.00050 wt%.

**Table 1.** Metal leaching and yield of Ru and/or Fe-biochar catalyst for hydrogenation of LA into GVL. Conditions for catalysis experiments: 4 mmol LA, 8 mmol FA, 0.50 g catalyst samples, 180 °C, and 3 h contact time.

| Catalyst | Yield GVL (%) | Leaching (wt%) | |
|---|---|---|---|
| | | Fe | Ru |
| $Fe_{500}$ | 3 | 4.61 | 0.000 |
| $BC_{500}$ | 0 | 0.06 | 0.000 |
| $BC_{500}Ru$ | 4 | 0.04 | 0.00050 |
| $BC_{500}Fe$ | 0 | 2.77 | 0.000 |
| $BC_{500}Fe3\%Ru$ (1° cycle) | 75 | 2.77 | 0.00026 |
| $BC_{500}Fe3\%Ru$ (2° cycles) | 71 | 1.58 | 0.00025 |
| $BC_{500}Fe3\%Ru$ (3° cycles) | 73 | 1.33 | 0.00018 |
| $BC_{500}Fe3\%Ru$ (4° cycle) | 63 | 1.84 | 0.00021 |
| $BC_{500}Fe3\%Ru$ (5° cycle) | 50 | 2.47 | 0.00032 |

In a comparable study, Zhang et al. (2018) [48] reported significantly higher Ru leaching values of 0.8 and 2.6 wt% for Ru/Ti and Ru/Al-Ti catalysts, respectively, during the complete conversion of LA in water at 80 °C and 4.0 MPa $H_2$. The values obtained in this study were approximately 4000 times lower than those reported by Zhang et al. (2018) [48].

Furthermore, the leaching of iron ions occurs after the conversion of LA under the optimized conditions. Notably, $Fe_{500}$ exhibited considerably higher leaching than $BC_{500}Fe$. This disparity may be attributed to the interactions between iron ions and biochar, preventing the significant leaching of iron ions into the solution. A similar phenomenon was observed by Kim et al. (2010) [49], where the introduction of 50 g $L^{-1}$ of Fe/Pd-alginate (3.7 g Fe $L^{-1}$) in an aqueous solution at 25 °C resulted in the release of metal from the support being <3% of the loaded iron.

EDS analysis corroborates the increased leaching observed after five cycles of the reaction, as detailed in Table S9 and Figure S7 in the Supplementary Information (SI). The data in Table S9 were subjected to variance analysis using the Student's *t*-test at the 0.05 probability level. The analysis revealed a significant difference in the content of oxygen, iron, and ruthenium (*p*-values of 0.0023, 0.0483, and 0.0074, respectively) when comparing $BC_{500}Fe3\%Ru$ before and after the five cycles of the reaction. The results of the *t*-test indicated that this significant difference is attributable to the leaching of iron and ruthenium. The decrease in oxygen content is consistent with the presence of iron and ruthenium in the form of oxides in the material, as further supported by the XPS analysis.

Table 1 presents an initial decreasing trend in the Fe content, from 2.77 wt% in the first cycle to 1.33 wt% in the third cycle, indicating the progressive stabilization of Fe species within the biochar matrix during early usage. However, from the fourth cycle onward, an increasing trend is observed, with the Fe content rising from 1.84 wt% to 2.47 wt%, suggesting the involvement of additional mechanisms. Based on the EDS analysis (Table S9 and Figure S7 in the SI) and XPS results discussed in Section 3.1, this behavior is likely associated with the reactivation of oxidized Fe species on the catalyst surface. This reactivation may be driven by structural rearrangements or the exposure of previously encapsulated Fe phases under repeated hydrothermal conditions. Furthermore, a measurable reduction in the surface oxygen content (Table S9) supports the hypothesis of complexation-induced Fe release, potentially arising from the degradation of oxygen-containing functional groups, such as carboxyl and hydroxyl groups, that initially contributed to Fe stabilization.

### *3.7. Effect of Triethylamine and Formate Loading on the LA Conversion to GVL Yield Production*

It is reported in the literature that the presence of a base in the conversion of LA to GVL in the presence of FA is considered essential for the hydrogenation reaction [5]. Feng et al. (2018) [5] demonstrated that the addition of triethylamine enhances the activity of ruthenium-based catalysts during the hydrogen generation from formic acid. This improvement is attributed to the presence of FA and LA in acidic forms. The introduction of a base in the reaction medium facilitates hydrogen transfer and minimizes the formation of by-products.

The results depicted in Figure 10 reveal that, contrary to the general trend reported in the literature, the addition of triethylamine does not enhance the activity of the $BC_{500}$Fe3%Ru catalyst in the conversion of LA and FA to GVL. As the quantity of triethylamine in the reaction medium increases, a decrease in the yield of GVL production is observed. This decline is attributed to the inhibitory effect of triethylamine, suggesting that an alkaline environment may impede the catalyst's activity. Shao Y. et al. (2022) [50] proposed that Brønsted acidic sites play a crucial role in facilitating the lactonization of 4-hydroxy pentanoic acid to form GVL. Therefore, triethylamine might be inhibiting these Brønsted acidic sites, hindering the lactonization process of 4-hydroxy pentanoic acid to form GVL [50].

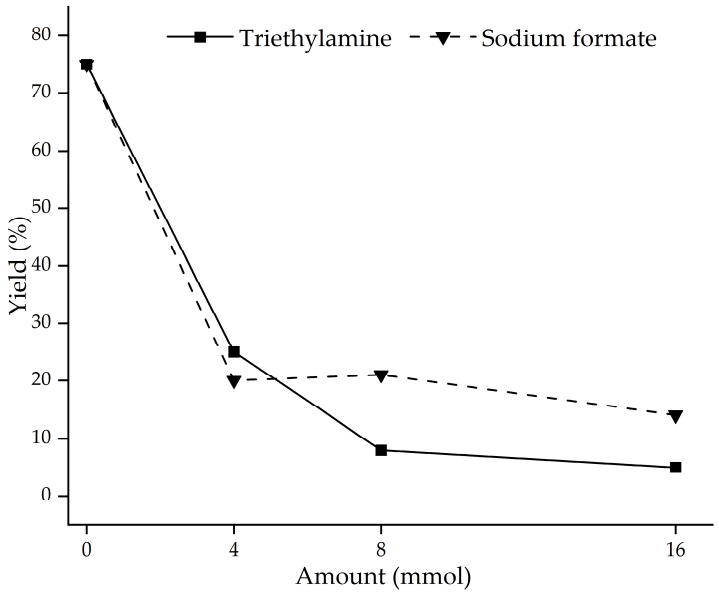



**Figure 10.** The effect of the presence of triethylamine and sodium formate on the conversion of LA to GVL. Conditions: 4 mmol LA, 8 mmol FA, 0.5 g $BC_{500}$Fe/3%Ru, 180 °C, 3 h.

Consequently, $BC_{500}$Fe3%Ru exhibits a notable efficiency in the base-free hydrogenation of LA to GVL in an aqueous medium containing formic acid.

Figure 10 also illustrates that, in the conversion of LA and FA to GVL facilitated by $BC_{500}$Fe3%Ru, the addition of sodium formate does not enhance the catalyst's activity. Similar to the effect observed with triethylamine, an increased amount of sodium formate results in a substantial decrease in conversion, plummeting from 73% to 14%. Gao et al. (2018) [13] elucidated that changes in pH due to sodium formate addition can influence the hydrogenation process. In their study, the authors noted an increase in pH from 1.83 to 4.05 upon the addition of potassium formate [13]. The decomposition of formate occurs with bicarbonate as the co-product: $HCOO^- + H_2O \Leftrightarrow H_2 + HCO_3^-$ [13]. The Ru/Fe-$HCO_3^-$ complex, involved in a deprotonation/protonation equilibrium, becomes prevalent as the pH rises during the reaction. Due to the stronger binding of bicarbonate to Ru than $CO_2$,

it exhibits a reduced release from the complex, consequently diminishing the catalytic activity [51].

### *3.8. Cost Estimates*

In Autumn 2018, the Chemical Catalysis for Bioenergy Consortium (ChemCatBio) introduced the "CatCost", an estimation tool available in spreadsheet and web formats. This tool provides detailed information for estimating the pre-commercial heterogeneous catalytic prices.

The estimated price of the $BC_{500}Fe/3\%Ru$ catalyst was determined using CatCost. Considering the envisioned application of the $BC_{500}Fe/3\%Ru$ catalyst in a large-scale LA hydrogenation plant with an assumed catalyst demand of 8 tons/year, the small-scale (1 ton/day) scenario was selected based on the relationships outlined in Excel SI, with a campaign length of 2.5 days, including cleaning. The total campaign cost, excluding materials, overhead, or margin, was calculated to be USD 25,584 by multiplying the step cost total by the campaign length (2.5 days).

To estimate the $BC_{500}Fe/3\%Ru$ catalyst price, the first step involved determining the raw material requirements, catalyst composition, and the laboratory-scale procedure for synthesis development. The $BC_{500}Fe/3\%Ru$ catalyst, as outlined in Section 2.2, was prepared through the wet impregnation/gelefication/pyrolysis of the biochar support (derived from sugarcane bagasse) with ruthenium chloride hydrate ($RuCl_3 \cdot xH_2O$). The equipment used for populating the raw material requirements is based on the process template: Metal on Metal Oxide—Incipient Wetness. Industrial-scale process equipment units, based on the lab-scale procedure, include incipient wetness, a multistep reactor, scrubber, plate and frame filter, simple reactor, heater (pyrolysis), and rotary dryer (40–100 °C).

The material costs are the highest, accounting for about 80% of the total cost. The base metal, ruthenium, is the most expensive component, accounting for about 50% of the total material cost. This is due to its scarcity and its unique catalytic properties. The auxiliary reagents, such as sodium alginate, account for about 10% of the total material cost. The other chemical materials account for about 40% of the total material cost. Capital and operating costs account for about 20% and 10% of the total administrative cost, respectively.

The estimated cost, inclusive of synthesis, overheads, and selling margin (refer to the Supplementary Information), was determined to be USD 5574.84/kg for $BC_{500}Fe/3\%Ru$. This is approximately half the commercial value for Ru/C (5%), which is USD 11,778.83/kg (Sigma Aldrich, accessed on 28 June 2024). Comparing the price and performance between studies featuring Ru/C (5%) and the development presented in this work, $BC_{500}Fe/3\%Ru$ demonstrates superior performance under conditions without additives and an estimated price, as described previously.

### *3.9. LA Conversion with Catalysts Is Reported in This Work and the Literature*

Table 2 illustrates a comparative analysis between the performance of BC500Fe/3%Ru and ruthenium-based catalysts under similar conditions. Notably, the catalysts investigated in this study exhibited superior performance. For instance, the 5 wt% Ru/C (Cl) catalyst, subjected to a high reduction temperature of 500 °C, yielded 57% GVL when tested at 190 °C for 5 h with a FA/LA ratio of 1:5. This result is nearly equivalent to the GVL yield obtained with $BC_{500}Fe/3\%Ru$, which underwent testing under less favorable conditions, involving an elevated temperature and extended reaction time.

In the case of the $TiO_2$-supported catalyst, the photo deposition method demonstrated efficacy, yielding a GVL yield of 49% compared to the incipient wet impregnation method, which yielded a lower value of 30%. However, both samples were tested under less favorable conditions, resulting in lower yields than the material synthesized in this study.

**Table 2.** Reaction conditions and results of GVL production with catalysts are reported in this work, and the literature is cited.

| Catalyst | LA/FA | Solvent | Catalyst Amount (g) | Metal Loading (%) | T (°C) | t (h) | GVL Yield (%) | TOF ($h^{-1}$) | TON | Ref. |
|---|---|---|---|---|---|---|---|---|---|---|
| $BC_{500}Fe/3\%Ru$ | 1:2 | $H_2O$ | 0.5 | 3 | 180 | 3 | 73 | 3.94 | 11.83 | This work |
| Ru/Ca-$TiO_2$ (incipient wet impregnation method) | 1:1 | $H_2O$ | 0.6 | 5 | 190 | 5 | 30 | 2.84 | 14.2 | [52] |
| Ru/Ca-$TiO_2$ (photodeposition method) | 1:1 | $H_2O$ | 0.6 | 5 | 190 | 5 | 49 | 1.74 | 8.69 | |
| Ru/C (commercial) | 1:2 | $H_2O$ | 0.2 | 5 | 160 | 3 | 8.96 | 6.04 | 18.11 | [5] |
| Ru/C (low reduction temperature of 200 °C) | 1:5 | $H_2O$ | 0.6 | 5 | 190 | 5 | 31 | 1.8 | 8.99 | [29] |
| Ru/C (high reduction temperature of 500 °C) | 1:5 | $H_2O$ | 0.6 | 5 | 190 | 5 | 45 | 2.61 | 13.04 | |
| Ru/C (Cl) (low reduction temperature of 200 °C) | 1:5 | $H_2O$ | 0.6 | 5 | 190 | 5 | 46 | 2.67 | 13.33 | |
| Ru/C (Cl) (high reduction temperature of 500 °C) | 1:5 | $H_2O$ | 0.6 | 5 | 190 | 5 | 57 | 3.31 | 16.53 | |
| PSCFZnPP (12-W LED light) | 2-propanol 1:3 | - | 0.01 | - | - | 16 | 72 | - | - | [53] |

The comprehensive analysis of Table 2 supports the conclusion that the biochar-derived material presented in this study holds significant promise. This promising performance is tentatively attributed to the adsorptive characteristics inherent in the biochar, fostering the proximity and interaction of formic acid molecules with active metal sites. This interaction facilitates the reaction and contributes to a higher LA conversion into GVL.

## 4. Conclusions

Bimetallic catalysts were synthesized from pyrolyzed sugarcane biomass, incorporating Ru/Fe particles through pyrolysis at varying temperatures. The resulting material was employed for the conversion of LA to GVL utilizing FA as the exclusive hydrogen source. The bimetallic catalyst, $BC_{500}Fe/3\%Ru$, prepared at 500 °C, exhibited satisfactory performance. Notably, $BC_{500}Fe/3\%Ru$ facilitated a GVL yield of 73% without the addition of triethylamine or sodium formate, as reported in previous studies utilizing Ru/C. The functionalization of the material's surface with Ru/Fe particles suggests their role in hydrogen dissociation and hydrogenation. Furthermore, the catalyst demonstrated consistent performance over three reaction cycles. Initial testing suggests that this catalyst may be a viable alternative, although further investigation is needed to validate its stability and large-scale applicability. This study highlights the potential of biochar as a catalytic support, contributing to the advancement of a biomass-based economy.

**Supplementary Materials:** The following supporting information can be downloaded at: https://www.mdpi.com/article/10.3390/biomass5020029/s1, Method S1: Characterization of the raw and modified biochars, Table S1: Summary of power catalysts; Table S2: Initial $2^{4-1}$ fractional

factorial design, providing the lower (−1), medium (0), and upper (+1) level values for each variable; Table S3: The fractional factorial design in terms of coded values; Table S4: Experimental response surface of central composite factor levels; Table S5: The response surface of central composite in terms of coded values; Table S6: XPS results for the chemical bond compositions (%) of carbon (C1s), ruthenium (Ru3d), oxygen (O1s), and iron (Fe2p) of $BC_{300}Fe/1\%Ru$, $BC_{300}Fe/5\%Ru$, $BC_{500}Fe/3\%Ru$, $BC_{700}Fe/1\%Ru$ and $BC_{700}Fe/5\%Ru$; Table S7: Analysis of variance (ANOVA) at $p$-value < 0.05 for the response surface of central composite for GVL production obtained; Table S8: Two-tailed $t$-test analysis ($\alpha = 0.05$) between predicted and experimental GVL yield; Table S9: Analysis of elemental composition of the $BC_{500}Fe/3\%Ru$ before and after reaction conversion LA to GVL. All results are expressed in percentage composition of the elements; Figure S1: The scheme of the synthesis of BC-Fe/Ru; Figure S2: SEM images of the $BC_{300}Fe/1\%Ru$. $BC_{300}Fe/5\%Ru$. $BC_{500}Fe/3\%Ru$. $BC_{700}Fe/1\%Ru$ and $BC_{700}Fe/5\%Ru$ samples before reaction; Figure S3: XPS deconvoluted spectra of (a) $BC_{300}Fe/1\%Ru$. (b) $BC_{300}Fe/5\%Ru$. (c) $BC_{500}Fe/3\%Ru$. (d) $BC_{700}Fe/1\%Ru$. (e) $BC_{700}Fe/5\%Ru$ samples; Figure S4: Pareto chart for $2^{4-1}$ fractional factorial design for the GVL production. The panels were obtained after implementing forward selection using $\alpha$-value to enter 0.05; Figure S5: The graph of effects versus expected normal value indicates each effect's influence on the production of GVL. Negligible effects are near zero, and essential effects are far from zero; Figure S6: GC-MS spectra for the transformation of LA to GVL. Conditions: 4 mmol LA, 8 mmol FA, 0.5 g catalyst, 180 °C, 3 h; Figure S7: SEM images of the $BC_{500}Fe/3\%Ru$ samples after reaction conversion of LA to GVL.

**Author Contributions:** Conceptualization, J.C.A.M. and A.H.R.; methodology, J.C.A.M. and A.H.R.; formal analysis, J.C.A.M.; investigation, J.C.A.M. and A.H.R.; resources, R.L. and A.H.R.; validation, J.C.A.M. and A.H.R.; visualization, J.C.A.M. and A.H.R.; writing—original draft preparation, J.C.A.M., R.L., M.S. and A.H.R.; writing—review and editing, J.C.A.M., R.L., M.S. and A.H.R.; supervision, A.H.R.; project administration, A.H.R.; funding acquisition, A.H.R. All authors have read and agreed to the published version of the manuscript.

**Funding:** This research was funded by Fundação de Amparo à Pesquisa do Estado de São Paulo, grant number 2016/08215-4, 2022/00985-6, Financiadora de Estudos e Projetos, grant number 01.22.0290.00 (0080/21), and Conselho Nacional de Desenvolvimento Científico e Tecnológico, grant number 141088/2020-6.

**Institutional Review Board Statement:** Not applicable.

**Informed Consent Statement:** Not applicable.

**Data Availability Statement:** Data are available on request due to restrictions, e.g., privacy or ethical: The data presented in this study are available on request from the corresponding author. The data are not publicly available due to ongoing research.

**Conflicts of Interest:** The authors declare no conflicts of interest.

## References

1. Lopez, G.; Keiner, D.; Fasihi, M.; Koiranen, T.; Breyer, C. From Fossil to Green Chemicals: Sustainable Pathways and New Carbon Feedstocks for the Global Chemical Industry. *Energy Environ. Sci.* **2023**, *16*, 2879–2909. [CrossRef]
2. Singh, N.; Singhania, R.R.; Nigam, P.S.; Dong, C.-D.; Patel, A.K.; Puri, M. Global Status of Lignocellulosic Biorefinery: Challenges and Perspectives. *Bioresour. Technol.* **2022**, *344*, 126415. [CrossRef] [PubMed]
3. Wang, Z.; Li, S.; Jin, Z.; Li, Z.; Liu, Q.; Zhang, K. Oil and Gas Pathway to Net-Zero: Review and Outlook. *Energy Strategy Rev.* **2023**, *45*, 101048. [CrossRef]
4. Huang, X.; Liu, K.; Vrijburg, W.L.; Ouyang, X.; Iulian Dugulan, A.; Liu, Y.; Tiny Verhoeven, M.W.G.M.; Kosinov, N.A.; Pidko, E.A.; Hensen, E.J.M. Hydrogenation of Levulinic Acid to γ-Valerolactone over Fe-Re/$TiO_2$ Catalysts. *Appl. Catal. B Environ.* **2020**, *278*, 119314. [CrossRef]
5. Feng, J.; Gu, X.; Xue, Y.; Han, Y.; Lu, X. Production of γ-Valerolactone from Levulinic Acid over a Ru/C Catalyst Using Formic Acid as the Sole Hydrogen Source. *Sci. Total Environ.* **2018**, *633*, 426–432. [CrossRef]
6. Mujtaba, M.; Fernandes Fraceto, L.; Fazeli, M.; Mukherjee, S.; Savassa, S.M.; Araujo de Medeiros, G.; do Espírito Santo Pereira, A.; Mancini, S.D.; Lipponen, J.; Vilaplana, F. Lignocellulosic Biomass from Agricultural Waste to the Circular Economy: A Review with Focus on Biofuels, Biocomposites and Bioplastics. *J. Clean. Prod.* **2023**, *402*, 136815. [CrossRef]

7. Li, X.; Li, J.; Liu, X.; Tian, Q.; Hu, C. The Promoting Effect of Ce on the Performance of Au/$Ce_xZr_{1-x}O_2$ for γ-Valerolactone Production from Biomass-Based Levulinic Acid and Formic Acid. *Catalysts* **2018**, *8*, 241. [CrossRef]
8. Khalid, M.; Granollers Mesa, M.; Scapens, D.; Osatiashtiani, A. Advances in Sustainable γ-Valerolactone (GVL) Production via Catalytic Transfer Hydrogenation of Levulinic Acid and Its Esters. *ACS Sustain. Chem. Eng.* **2024**, *12*, 16494–16517. [CrossRef]
9. Raspolli Galletti, A.M.; Licursi, D.; Ciorba, S.; Di Fidio, N.; Coccia, V.; Cotana, F.; Antonetti, C. Sustainable Exploitation of Residual *Cynara cardunculus* L. to Levulinic Acid and n-Butyl Levulinate. *Catalysts* **2021**, *11*, 1082. [CrossRef]
10. Li, X.; Shi, X.-L.; Wang, J.; Shi, K.; Wang, Q. Effect of Different Hydrogen Donors on the Catalytic Conversion of Levulinic Acid to γ-Valerolactone over Non-Noble Metal Catalysts. *J. Ind. Eng. Chem.* **2024**, *138*, 17–33. [CrossRef]
11. Hijazi, A.; Khalaf, N.; Kwapinski, W.; Leahy, J. Catalytic Valorisation of Biomass Levulinic Acid into Gamma Valerolactone Using Formic Acid as a H 2 Donor: A Critical Review. *RSC Adv.* **2022**, *12*, 13673–13694. [CrossRef] [PubMed]
12. Valentini, F.; Kozell, V.; Petrucci, C.; Marrocchi, A.; Gu, Y.; Gelman, D.; Vaccaro, L. Formic Acid, a Biomass-Derived Source of Energy and Hydrogen for Biomass Upgrading. *Energy Environ. Sci.* **2019**, *12*, 2646–2664. [CrossRef]
13. Gao, Y.; Zhang, H.; Han, A.; Wang, J.; Tan, H.R.; Tok, E.S.; Jaenicke, S.; Chuah, G.K. Ru/$ZrO_2$ Catalysts for Transfer Hydrogenation of Levulinic Acid with Formic Acid/Formate Mixtures: Importance of Support Stability. *ChemistrySelect* **2018**, *3*, 1343–1351. [CrossRef]
14. Ramos, R.; Abdelkader-Fernández, V.K.; Matos, R.; Peixoto, A.F.; Fernandes, D.M. Metal-Supported Biochar Catalysts for Sustainable Biorefinery, Electrocatalysis, and Energy Storage Applications: A Review. *Catalysts* **2022**, *12*, 207. [CrossRef]
15. Phule, A.D.; Zaman, M.W.U.; Elkaee, S.; Kim, S.Y.; Lee, S.G.; Park, G.; Yang, J.H. Carbon-Based Catalysts for Clean Environmental Remediation. *Int. J. Environ. Res.* **2023**, *18*, 3. [CrossRef]
16. Gholizadeh, M.; Meca, S.; Zhang, S.; Clarens, F.; Hu, X. Understanding the Dependence of Biochar Properties on Different Types of Biomass. *Waste Manag.* **2024**, *182*, 142–163. [CrossRef]
17. Wang, L.; Wang, J.; Yan, W.; He, C.; Shi, Y. $MgFe_2O_4$-Biochar Based Lanthanum Alginate Beads for Advanced Phosphate Removal. *Chem. Eng. J.* **2020**, *387*, 123305. [CrossRef]
18. Serrano-Ruiz, J.C.; Braden, D.J.; West, R.M.; Dumesic, J.A. Conversion of Cellulose to Hydrocarbon Fuels by Progressive Removal of Oxygen. *Appl. Catal. B Environ.* **2010**, *100*, 184–189. [CrossRef]
19. Muñiz-Márquez, D.B.; Wong-Paz, J.E.; Contreras-Esquivel, J.C.; Rodriguez-Herrera, R.; Aguilar, C.N. Extraction of Phenolic Compounds From *Coriandrum sativum* L. and *Amaranthus hybridus* L. by Microwave Technology. *Polyphen. Plants* **2019**, 185–190. [CrossRef]
20. Baddour, F.G.; Snowden-Swan, L.; Super, J.D.; Van Allsburg, K.M. Estimating Precommercial Heterogeneous Catalyst Price: A Simple Step-Based Method. *Org. Process Res. Dev.* **2018**, *22*, 1599–1605. [CrossRef]
21. Allsburg, K.M.V.; Tan, E.C.D.; Super, J.D.; Schaidle, J.A.; Baddour, F.G. Early-Stage Evaluation of Catalyst Manufacturing Cost and Environmental Impact Using CatCost. *Nat. Catal.* **2022**, *5*, 342–353. [CrossRef]
22. Yu, C.; Wang, M.; Dong, X.; Shi, Z.; Zhang, X.; Lin, Q. Removal of Cu(II) from Aqueous Solution Using Fe3O4–Alginate Modified Biochar Microspheres. *RSC Adv.* **2017**, *7*, 53135–53144. [CrossRef]
23. Du, Q.; Li, G.; Zhang, S.; Song, J.; zhao, Y.; Yang, F. High-Dispersion Zero-Valent Iron Particles Stabilized by Artificial Humic Acid for Lead Ion Removal. *J. Hazard. Mater.* **2020**. [CrossRef] [PubMed]
24. Noraini, M.N.; Abdullah, E.C.; Othman, R.; Mubarak, N.M. Single-Route Synthesis of Magnetic Biochar from Sugarcane Bagasse by Microwave-Assisted Pyrolysis. *Mater. Lett.* **2016**, *184*, 315–319. [CrossRef]
25. Huang, J.; Yang, S.; Xu, Y.; Zhou, X.; Jiang, X.; Shi, N.; Cao, D.; Yin, J.; Wang, G. Fe2O3 Sheets Grown on Nickel Foam as Electrode Material for Electrochemical Capacitors. *J. Electroanal. Chem.* **2014**, *713*, 98–102. [CrossRef]
26. Zhou, X.; Wang, Q.; Guo, Y.; Sun, X.; Li, T.; Yang, C. Spectroscopic Characterization of Dissolved Organic Matter from Macroalgae Ulva Pertusa Decomposition and Its Binding Behaviors with Cu(II). *Ecotoxicol. Environ. Saf.* **2021**, *225*, 112811. [CrossRef]
27. Wu, J.; Zeng, R.J.; Zhang, F.; Yuan, Z. Application of Iron-Crosslinked Sodium Alginate for Efficient Sulfide Control and Reduction of Oilfield Produced Water. *Water Res.* **2019**, *154*, 12–20. [CrossRef] [PubMed]
28. Eslami, S.; Ebrahimzadeh, M.A.; Biparva, P. Green Synthesis of Safe Zero Valent Iron Nanoparticles by Myrtus Communis Leaf Extract as an Effective Agent for Reducing Excessive Iron in Iron-Overloaded Mice, a Thalassemia Model. *RSC Adv.* **2018**, *8*, 26144–26155. [CrossRef]
29. Ruppert, A.M.; Jędrzejczyk, M.; Sneka-Płatek, O.; Keller, N.; Dumon, A.S.; Michel, C.; Sautet, P.; Grams, J. Ru Catalysts for Levulinic Acid Hydrogenation with Formic Acid as a Hydrogen Source. *Green Chem.* **2016**, *18*, 2014–2028. [CrossRef]
30. Liang, H.; Zhu, C.; Ji, S.; Kannan, P.; Chen, F. Magnetic $Fe_2O_3$/Biochar Composite Prepared in a Molten Salt Medium for Antibiotic Removal in Water. *Biochar* **2022**, *4*, 3. [CrossRef]
31. Macedo, J.C.A.; Gontijo, E.S.J.; Herrera, S.G.; Rangel, E.C.; Komatsu, D.; Landers, R.; Rosa, A.H. Organosulphur-Modified Biochar: An Effective Green Adsorbent for Removing Metal Species in Aquatic Systems. *Surf. Interfaces* **2021**, *22*, 100822. [CrossRef]
32. Bardestani, R.; Biriaei, R.; Kaliaguine, S. Hydrogenation of Furfural to Furfuryl Alcohol over Ru Particles Supported on Mildly Oxidized Biochar. *Catalysts* **2020**, *10*, 934. [CrossRef]

33. Morgan, D.J. Resolving Ruthenium: XPS Studies of Common Ruthenium Materials. *Surf. Interface Anal.* **2015**, *47*, 1072–1079. [CrossRef]
34. Singh, B.K.; Kim, Y.; Kwon, S.; Na, K. Selective Catalytic Transfer Hydrogenolysis of Glycerol to 2-Isopropoxy-Propan-1-Ol over Noble Metal Ion-Exchanged Mordenite Zeolite. *Catalysts* **2019**, *9*, 885. [CrossRef]
35. Chen, D.; Zheng, Z.; Zhang, F.; Ke, R.; Sun, N.; Wang, Y.; Wang, Y. Fe@$Fe_2O_3$-Loaded Biochar as an Efficient Heterogeneous Fenton Catalyst for Organic Pollutants Removal. *Water Sci. Technol.* **2022**, *85*, 2797–2810. [CrossRef]
36. Li, P.; Jiang, E.Y.; Bai, H.L. Fabrication of Ultrathin Epitaxial γ-$Fe_2O_3$ Films by Reactive Sputtering. *J. Phys. D Appl. Phys.* **2011**, *44*, 075003. [CrossRef]
37. Oladipo, A.A.; Ifebajo, A.O. Highly Efficient Magnetic Chicken Bone Biochar for Removal of Tetracycline and Fluorescent Dye from Wastewater: Two-Stage Adsorber Analysis. *J. Environ. Manag.* **2018**, *209*, 9–16. [CrossRef]
38. Su, J.-Z.; Wang, C.-C.; Zhang, M.-Y.; Zong, X.-B.; Huang, X.-F.; Deng, Z.-H.; Xiang, P. Advances and Prospectives of Iron/Biochar Composites: Application, Influencing Factors and Characterization Methods. *Ind. Crops Prod.* **2023**, *205*, 117496. [CrossRef]
39. Mihet, M.; Dan, M.; Barbu-Tudoran, L.; Lazar, M.D.; Blanita, G. Controllable $H_2$ Generation by Formic Acid Decomposition on a Novel Pd/Templated Carbon Catalyst. *Hydrogen* **2020**, *1*, 22–37. [CrossRef]
40. Yu, Z.; Lu, X.; Xiong, J.; Li, X.; Bai, H.; Ji, N. Heterogeneous Catalytic Hydrogenation of Levulinic Acid to γ-Valerolactone with Formic Acid as Internal Hydrogen Source. *ChemSusChem* **2020**, *13*, 2916–2930. [CrossRef]
41. Chen, H.; Xu, Q.; Li, H.; Liu, J.; Liu, X.; Huang, G.; Yin, D. Catalytic Transfer Hydrogenation of Ethyl Levulinate to γ-Valerolactone over Ni Supported on Equilibrium Fluid-Catalytic-Cracking Catalysts. *Catal. Lett.* **2021**, *151*, 538–547. [CrossRef]
42. Alabi, O.; Olanrewaju, A.A.; Afolabi, T.J. Process Optimization of Adsorption of Cr(VI) on Adsorbent Prepared from Bauhinia Rufescens Pod by Box-Behnken Design. *Sep. Sci. Technol.* **2019**, *55*, 47–60. [CrossRef]
43. Elazazy, M.S.; Issa, A.A.; Al-Mashreky, M.; Al-Sulaiti, M.; Al-Saad, K. Application of Fractional Factorial Design for Green Synthesis of Cyano-Modified Silica Nanoparticles: Chemometrics and Multifarious Response Optimization. *Adv. Powder Technol.* **2018**, *29*, 1204–1215. [CrossRef]
44. Rodríguez, V.I.; Mendow, G.; Sánchez, B.S.; García, J.R.; Pujro, R.A.; de Miguel, S.R.; Veizaga, N.S. Ruthenium Catalysts Supported on Hydrothermally Treated Carbon from Rice Husk: The Effect of Reduction Temperature on the Hydrogenation Reaction of Levulinic Acid to γ-Valerolactone. *Processes* **2023**, *11*, 1421. [CrossRef]
45. Ibrahim, A.; Liu, X.; Uguna, C.N.; Sun, C. Selective Hydrogenation of Levulinic Acid to γ-Valerolactone over Copper Based Bimetallic Catalysts Derived from Metal-Organic Frameworks. *Mater. Today Sustain.* **2023**, *23*, 100424. [CrossRef]
46. Jing, P.; Gan, T.; Qi, H.; Zheng, B.; Chu, X.; Yu, G.; Yan, W.; Zou, Y.; Zhang, W.; Liu, G. Synergism of Pt Nanoparticles and Iron Oxide Support for Chemoselective Hydrogenation of Nitroarenes under Mild Conditions. *Chin. J. Catal.* **2019**, *40*, 214–222. [CrossRef]
47. Shi, H.; Lu, Z.; Xu, H.; Wang, S.; Nian, B.; Hu, Y. Selective and Efficient Synthesis of Pine Sterol Esters Catalyzed by Deep Eutectic Solvent. *Molecules* **2023**, *28*, 993. [CrossRef]
48. Zhang, L.; Mao, J.; Li, S.; Yin, J.; Sun, X.; Guo, X.; Song, C.; Zhou, J. Hydrogenation of Levulinic Acid into Gamma-Valerolactone over in Situ Reduced CuAg Bimetallic Catalyst: Strategy and Mechanism of Preventing Cu Leaching. *Appl. Catal. B Environ.* **2018**, *232*, 1–10. [CrossRef]
49. Kim, H.; Hong, H.J.; Jung, J.; Kim, S.H.; Yang, J.W. Degradation of Trichloroethylene (TCE) by Nanoscale Zero-Valent Iron (nZVI) Immobilized in Alginate Bead. *J. Hazard. Mater.* **2010**, *176*, 1038–1043. [CrossRef]
50. Shao, Y.; Ba, S.; Sun, K.; Gao, G.; Fan, M.; Wang, J.; Fan, H.; Zhang, L.; Hu, X. Selective Production of γ-Valerolactone or 1,4-Pentanediol from Levulinic Acid/Esters over Co-Based Catalyst: Importance of the Synergy of Hydrogenation Sites and Acidic Sites. *Chem. Eng. J.* **2022**, *429*, 132433. [CrossRef]
51. Fellay, C.; Yan, N.; Dyson, P.J.; Laurenczy, G. Selective Formic Acid Decomposition for High-Pressure Hydrogen Generation: A Mechanistic Study. *Chem.—A Eur. J.* **2009**, *15*, 3752–3760. [CrossRef] [PubMed]
52. Wojciechowska, J.; Jędrzejczyk, M.; Grams, J.; Keller, N.; Ruppert, A.M. Enhanced Production of γ-Valerolactone with an Internal Source of Hydrogen on Ca-Modified $TiO_2$ Supported Ru Catalysts. *ChemSusChem* **2019**, *12*, 639–650. [CrossRef] [PubMed]
53. Khajone, V.B.; Raut, S.U.; Deshmukh, S.A.; Bhansali, K.J.; Balinge, K.R.; Muskawar, P.N.; Bhagat, P.R. Recyclable Polymer-Supported Carboxyl Functionalized Zn–Porphyrin Photocatalyst for Transfer Hydrogenation of Levulinic Acid to γ-Valerolactone. *Biomass Convers. Biorefinery* **2023**, *13*, 9107–9117. [CrossRef]


**Disclaimer/Publisher's Note:** The statements, opinions and data contained in all publications are solely those of the individual author(s) and contributor(s) and not of MDPI and/or the editor(s). MDPI and/or the editor(s) disclaim responsibility for any injury to people or property resulting from any ideas, methods, instructions or products referred to in the content.